Applied Materials Today 21 (2020) 100866

Contents lists available at ScienceDirect

Applied Materials Today

journal homepage: www.elsevier.com/locate/apmt

Ultrasonic plasticity of metallic glass near room temperature

X. Li[a,1], D. Wei[b,1], J.Y. Zhang[c,1], X.D. Liu[a], Z. Li[a], T.Y. Wang[c], Q.F. He[c], Y.J. Wang[b,d,*], J. Ma[a,**], W.H. Wang[e,f], Y. Yang[c,g,***]

[a] College of Mechatronics and Control Engineering, Shenzhen University, Shenzhen 518060, China
[b] State Key Laboratory of Nonlinear Mechanics, Institute of Mechanics, Chinese Academy of Sciences, Beijing 100190, China
[c] Department of Mechanical Engineering, College of Engineering, City University of Hong Kong, Kowloon Tong, Kowloon, Hong Kong, China
[d] School of Engineering Science, University of Chinese Academy of Sciences, Beijing 100049, China
[e] Institute of Physics, Chinese Academy of Sciences, Beijing 100190, China
[f] Songshan Lake Materials Laboratory, Dongguan 523808, China
[g] Department of Materials Science and Engineering, College of Engineering, City University of Hong Kong, Kowloon Tong, Kowloon, Hong Kong, China

ARTICLE INFO

Article history:
Received 15 September 2020
Revised 20 October 2020
Accepted 21 October 2020

Keywords:
Metallic glass
Ultrasound agitated super-plasticity
Room temperature deformation
Atomic-scale dilations
Dynamic heterogeneity

ABSTRACT

Bulk metallic glasses (BMGs) are well-known for their superb strength (1–4 GPa) (Ashby and Greer, 2006) [1] but poor/localized plasticity when deformed at low temperatures or high strain rates (Inoue and Takeuchi, 2011; Kumar et al., 2009) [2,3]. Therefore, processing of BMGs, such as forming and shaping for various important applications, is usually performed above their glass transition temperatures (T_g) – also known as "thermo-plastic" forming (Geer, 1995) – for which the selection of alloy composition and the protocol for thermal treatment is demanding in order to promote extensive homogeneous plastic flows while avoiding crystallization (Geer, 1995). In stark contrast, here we demonstrate that homogeneous super-plasticity can occur rapidly in different BMGs below their T_g when subjected to ultrasonic agitations. Through atomistic simulations and nanomechanical characterization, we provide the compelling evidence to show that this super-plasticity is attributed to dynamic heterogeneity and cyclic induced atomic-scale dilations in BMGs, which leads to significant rejuvenation and final collapse of the solid-like amorphous structure, thereby leading to an overall fluid-like behavior. Our finding uncovers that BMGs can undergo substantial plastic flows through unusual liquefaction near room temperature and, more importantly, it leads to the development of a facile and cost-effective "ultrasonic-plastic" forming method to process a wide range of BMGs at low temperatures.

1. Introduction

Owing to their amorphous structure, bulk metallic glasses (BMGs) possess superb strength, excellent elastic strain limit and superior corrosion resistance; therefore, they have been attracting tremendous research interest because of their potential use for various engineering applications [5–7]. However, like many other high strength materials, such as nanocrystalline metals, BMGs are plagued with low plasticity, particularly at low temperatures; therefore, processing of BMGs, such as forming, shaping and forging, is usually performed above their glass transition temperature (T_g) and within the supercooled liquid region such that super-plasticity can occur in the process known as thermo-plastic forming (TPF) [7,8] due to the liquefaction of BMGs. From the technological viewpoint, TPF is of great importance and has resulted in many novel applications of BMGs [7], however, it is applicable only to a few compositions which have a wide supercooled liquid region and good thermal stability to endure long time spans without crystallization and oxidation [7]. Surprisingly, here we demonstrate that, even without raising the temperature above T_g, BMGs can be liquefied by ultrasound, which leads to super-plastic flows and "ultrasonic-plastic" forming (UPF) near room temperature.

2. Results and discussions

Fig. 1(a) shows the schematics for the experimental set-up of the ultrasonic plasticity experiments we designed for BMGs. During the experiments, a BMG sample was placed right under the

* Corresponding author at: State Key Laboratory of Nonlinear Mechanics, Institute of Mechanics, Chinese Academy of Sciences, Beijing 100190, China.
** Corresponding author at: College of Mechatronics and Control Engineering, Shenzhen University, Shenzhen 518060, China.
*** Corresponding author at: Department of Mechanical Engineering, College of Engineering, City University of Hong Kong, Kowloon Tong, Kowloon, Hong Kong, China.
E-mail addresses: yjwang@imech.ac.cn (Y.J. Wang), majiang@szu.edu.cn (J. Ma), yonyang@cityu.edu.hk (Y. Yang).
[1] These authors contributed equally to this work.

https://doi.org/10.1016/j.apmt.2020.100866
2352-9407/

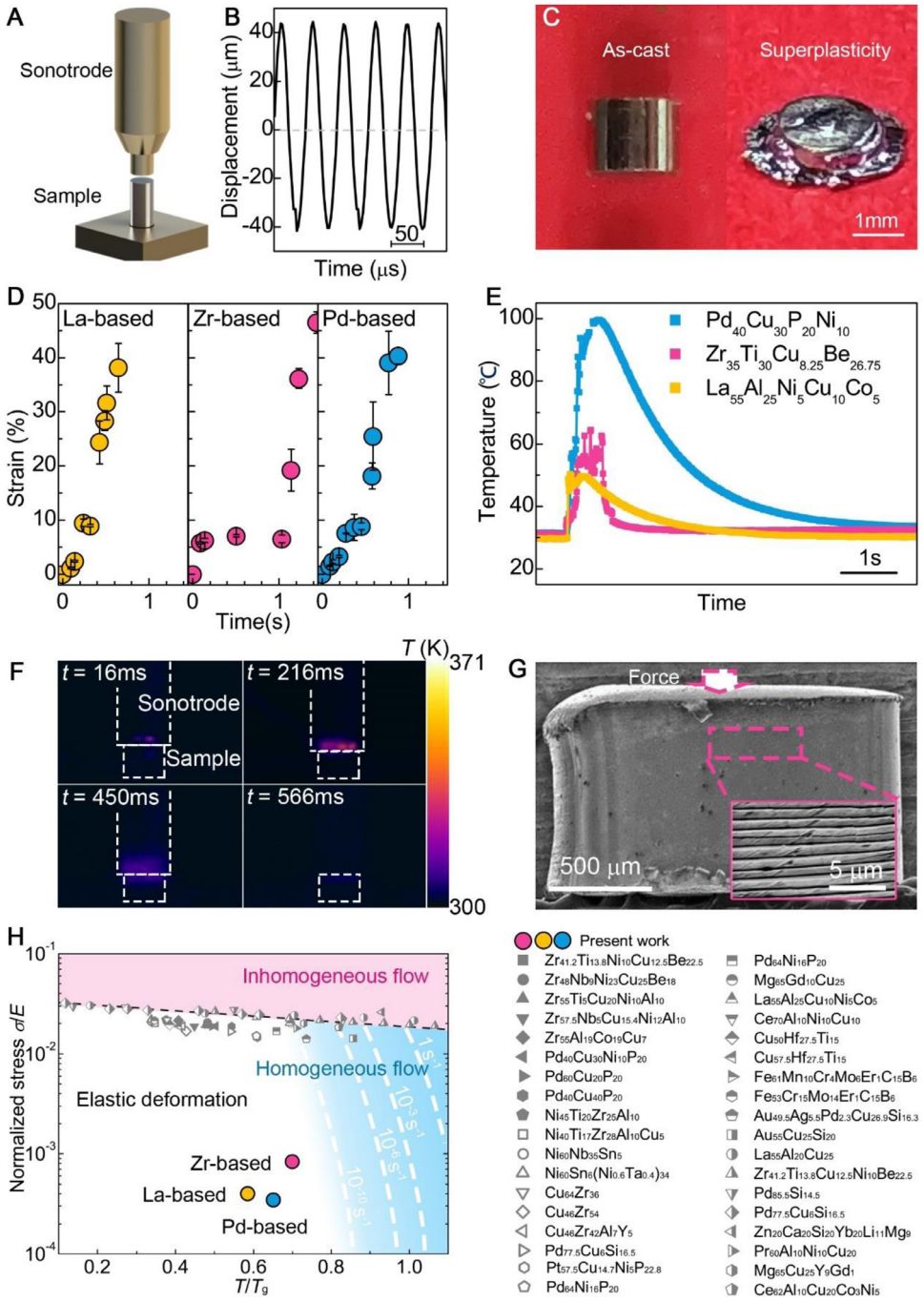

Fig. 1. Ultrasonic plasticity of metallic glasses. (a) Schematic diagram of the experimental set-up. (b) The displacement of the sonotrode during the ultrasonic vibration. (c) The comparison of BMGs before and after ultrasonic plasticity. (d) The strain versus time curves of La-based, Pd-based and Zr-based metallic glass, respectively. (e) Temperature change during the ultrasonic plasticity of different BMGs. (f) The infrared images of the BMG during the ultrasonic vibrations. (g) The wrinkling structures induced by the ultrasonic vibrations. (h) Deformation map for metallic glasses in stress–temperature axes. The data points from others work are taken from [Refs. 10,11].

sonotrode on a base plate made of cemented carbide. A very low static pre-pressure (12 MPa) was applied onto the BMG sample through the sonotrode for tight clamping. After that, the sonotrode oscillated with displacement control at a frequency of 20,000 Hz. As shown by Fig. 1(b), the oscillation of the sonotrode follows a sinusoidal function with amplitude of 44.4 μm. In principle, the total cyclic displacement is the sum of the machine displacement amplitude and the sample displacement amplitude. After correcting the machine compliance effect, we found that the peak stress corresponding to the cyclic displacement (Fig. 1(b)) was about 35 MPa (see Methods), well below the yield strengths (1–4 GPa) of BMGs [4].

Interestingly, with the increasing time for the ultrasonic agitation, the BMG underwent significant “acoustic softening” and kept deforming in a fluid-like manner, as seen in Fig. 1(c and d). Within around one second, the measured plastic strain already reached 50%. Note that this unusual fluid-like behavior was observed in different BMGs, such as La-, Pd- and Zr-based BMGs. After the ultrasonic experiments, we examined the sonotrode-sample contact but did not found any cracking (Supplementary Fig. S1). Note that similar findings of super-plasticity were observed in multiple samples with different heights and strains (Supplementary Fig. S2a). Fig. 1(c) compares the morphology of the BMG sample before and after the ultrasonic agitation induced super-plasticity. Evidently,

the overall plastic flow occurred in a homogeneous manner. Subsequently, we examined the structure of the deformed BMG samples with X-ray diffraction (XRD). The XRD results clearly show that even the most severely deformed BMGs remain amorphous without any sign of crystallization (Supplementary Fig. S2b). Here, it is noteworthy that the ultrasonic agitations result in super-plasticity only in a fully amorphous sample; by contrast, they cause fracture if the sample was crystallized (Supplementary Fig. S2c, Supplementary Video S1).

To probe the underlying physical mechanism, we first measured the instant temperature of the BMG samples using a thermocouple during the ultrasonic experiment (see Methods). As seen in Fig. 1(e), the temperature rose rapidly once the ultrasonic experiment started, reached a peak in the middle and declined gradually as the sample and sonotrode disengaged. Note that the measured peak temperature varies with the sample composition. According to our experiments, the measured peak temperature was 51 °C for the La-based BMG, 65 °C for the Zr-based BMG and 100 °C for the Pd-based BMG. Notably, this temperature rise is inadequate to reach T_g of the BMGs. To substantiate this finding, we videotaped the ultrasonic experiments with an infrared camera (see Methods and Supplementary Video S2). As seen in Fig. 1(f), the thermal images clearly show that the overall temperature is much lower than T_g, which is consistent with the previous results measured through the thermocouple. For comparison, we compressed the BMGs in a quasi-static experiment at the temperatures equal to the recorded peak temperatures (see Methods). As shown in Supplementary Fig. S3, the BMGs did not show any sign of super-plasticity but fractured in a brittle manner. Thus, these results indicate that the observed "acoustic softening" is not due to thermal rise.

After the occurrence of ultrasound agitated super-plasticity, we examined the post-deformation morphologies of the BMG samples with scanning electron microscopy (SEM) (Fig. 1(g)). Interestingly, we observed massive wrinkles wrapping around the deformed samples at the early stage of super-plasticity (inset of Fig. 1(g)), which is atypical if compared to localized shear banding in quasi-static compression. However, a similar phenomenon of wrinkling was often observed on flowing lava, which cools on its surface first and within its bulk afterwards [9]. According to the literature [10,11], high strain rate may promote plasticity in BMGs. However, since the applied stress in our present work is within the ordinary elastic region, the mechanism of yielding under ultrasonic agitation is different from the conventional yielding mechanism under quasi-static loadings. Fig. 1(h) shows a typical deformation map constructed based on the data obtained from quasi-static experiments [12,13], based on which one can infer that BMGs should deform in an elastic manner for a small stress, a low homologous temperature, and a high strain rate. It is evident that our findings contradict this conventional wisdom and hence, uncover a hidden flow yet to be understood.

First, let us estimate the temperature rise with the theoretical model established for anelasticity or β relaxations in BMGs [14] by neglecting the friction at the sample-sonotrode contact. In principle, temperature can increase in a cylindric BMG sample due to the heat generated by anelasticity, which is simultaneously conducted away into the ambient. In theory, the steady-state temperature rise ΔT depends on the loss modulus $G''$of BMGs [14,15], which can be expressed as:

$$G'' = \frac{2\nu e^{-\frac{\Delta G}{k_B T}} \beta\Omega\mu^2\omega k_B T}{\left(2\nu e^{-\frac{\Delta G}{k_B T}} (\beta\Omega\mu + k_B T)\right)^2 + (\omega k_B T)^2}$$

where k_B= the Boltzmann constant, T = the ambient temperature, ω = the angular frequency of external agitation, ΔG = the activation energy of local relaxation event, ν = attempt frequency of local relaxation sites, μ = the unrelaxed modulus (~25 GPa) and $\beta\Omega$ = the effective activation volume of local stress relaxation events; which can be taken as ~5 $\times 10^{-6}$nm^3 according to [Ref. 14]. Taking $T = 288$ K and $\omega = 6.28 \times 10^4$ Hz, we can thus obtain ΔT for different ΔG and ν, as shown in Fig. 2(a). Since 0.35 eV $< \Delta G <$ 0.47 eV [16], and ν, i.e., 1×10^{11} Hz $< \nu <$ 4×10^{11} Hz[17], we estimate that 50 $K < \Delta T <$ 100 K, which agrees with our experimental results (Fig. 1(c)).

Next, we measured the local elastic modulus of the BMG samples before and after the ultrasonic experiments (see Methods). For comparison, we also took the same measurements on the samples quasi-statically deformed at the same temperature as the peak temperature measured in the ultrasonic experiments (hereinafter referred to as thermal plasticity). As seen in Fig. 2(b and c), compared to the as-cast sample, the local elastic moduli of the Pd-based BMG reduce significantly after ultrasonic plasticity but increase after thermal plasticity. A similar phenomenon was also observed on the La-based and Zr-based BMGs (Supplementary Fig. S4). In addition, we performed nanoindentation tests at the loading rate of 500 μN/s on the different BMG samples. The nanoindentation load–displacement curves clearly show that localized plasticity in nanoindentation is suppressed by the ultrasonic super-plasticity but enhanced by the thermal plasticity (Supplementary Fig. S5). According to Refs. [18–20], these results indicate that there the structure of the BMG samples was rejuvenated after ultrasonic plasticity but relaxed after thermal plasticity.

Fig. 2(d) shows the results of differential scanning calorimetry (DSC) obtained for the Pd-based BMG samples (see Methods). Notable, the heat of excess relaxation enthalpy (ΔH_{rel}) increases from 0.11 kJ•mol^{-1} to 0.26 kJ•mol^{-1} after ultrasonic plasticity, but reduces significantly to 0.08 kJ•mol^{-1} after thermal plasticity. The same trend of ΔH_{rel} variation was also seen in the La-based and Zr-based BMGs (Supplementary Fig. S4). Fig. 2(e) presents the high-resolution transmission electron microscopy (HRTEM) images of the Pd-based samples (see Methods). Clearly, all samples remain amorphous; however, we note that the radius of the halo ring corresponding to the selective area diffraction pattern (SADP; insets of Fig. 2(e and f)) increases after thermal plasticity but decreases after ultrasonic plasticity. Since the radius is inversely proportional to average atomic spacing [21], these results indicate that the amorphous structure became more loosely packed, in agreement with rejuvenation, after ultrasonic plasticity but more densely packed, in agreement with relaxation, after thermal plasticity. We note that this behavior is consistent with the results reported in Ref. [22, 23], in which cyclic loading in the apparent elastic regime resulted in structural rejuvenation of metallic glasses.

Furthermore, we performed systematic molecular dynamics (MD) simulations on a $Cu_{50}Zr_{50}$ model glass system to elucidate the atomic-scale mechanism of ultrasonic plasticity. To accelerate the dynamic process of cyclic softening, symmetric tension-compression cyclic strain with a magnitude of 0.05 was applied with the strain rate of 10^9 s^{-1} for a total of 100 cycles. As seen in Fig. 3, our MD simulations clearly reveal prominent structural and energetic rejuvenation of the model glass, being consistent with our experimental observations. Note that strain amplitudes other than 0.05 were also used in our simulations. The general trend is that the smaller is the strain amplitude the longer is the waiting time for significant cyclic softening. As seen in Supplementary Figure S6, an apparent liquid flow can be readily caused by a large strain magnitude within the limited time window.

Fig. 3(a–d) illustrates the evolution of modulus, potential energy and tensile peak stress, respectively, as a function of cyclic number. The reduction in stiffness echoes well with the decreasing modulus we measured on the deformed sample (see Fig. 2(band c)). In addition, we observed the decrease in applied stress and the increase in potential energy after cyclic deformation, all of which indicate structural and thermodynamic rejuvenation [19,20,24]. Fig. 3(e and

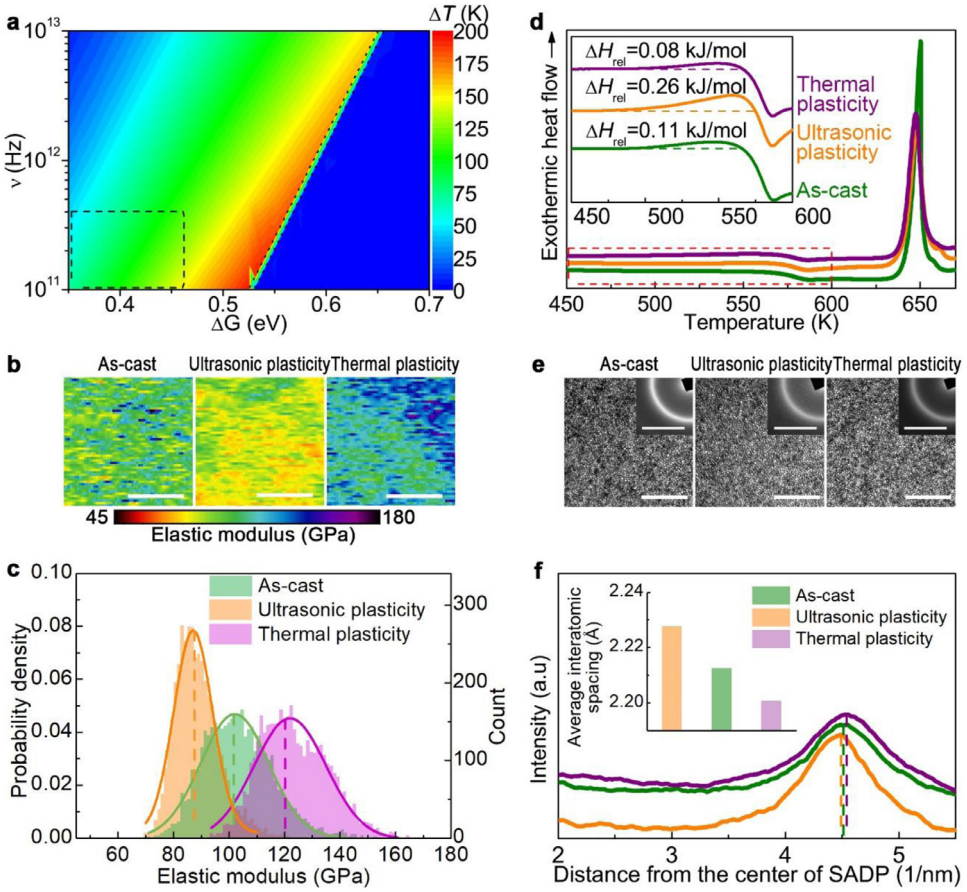

Fig. 2. Mechanical and structural characterization of Pd-based metallic glass under different conditions. (a) Contour of estimated temperature increment as a function of attempting frequency and activation energy. (b) Dynamic modulus mapping on the surface of Pd-based samples (scale bar=100 nm), (c) Moduli distributions of (b). (d) Representative DSC traces. Inset shows the close-up view of the relaxation exotherm. (e) HRTEM images and corresponding SADPs of the Pd-based BMGs, (the scale bar = 5 nm for TEM images while 5 nm^{-1} for SADP) (f) Electron diffraction intensity profiles extracted from the SADPs. Inset shows the corresponding average interatomic spacing.

f) shows the variation of the features of the potential energy landscape (PEL) induced by the cyclic loadings. Evidently, the spatial distribution of activation energy shows substantial increase in the low activation energy regime after $N = 100$ cycles, implying an increased volume fraction of active "flow units" [10]. The activation energy spectra also demonstrate an increase in the left tail of the low barrier events, all of which consistently reveal a rejuvenated state that possesses more potential shear transition zones [17,25] after cycling.

Now the question is: How does the cyclic deformation causes continuous rejuvenation and ultimately liquefaction in BMGs? In the literature of amorphous solids [26], such as granular matters, cyclic-loading induced liquefaction is known to be caused by the cycling induced excessive pressure around "liquid-like" sites, which accumulates and finally collapses the whole amorphous structure if no sufficient time is allowed for stress relaxation. In Fig. 3(h–i) we plot the evolution of atomic von Mises shear strain $\langle \eta_i^{\text{Mises}} \rangle$ and volumetric strain $\langle \delta_i \rangle$, respectively. While all strain measures, together with the nonaffine squared displacement (Supplementary Figs.S7 and S8, and Supplementary Video S3) increase with the strain cycles, the ratio between the volumetric strain to shear train, $\langle \delta_i \rangle / \langle \eta_i^{\text{Mises}} \rangle$, clearly indicates that the volumetric strain increases more rapidly than the shear strain. To further pinpoint the mechanism, we calculated the spatial autocorrelation function of strains, $C(r)$, at different cyclic number, as shown in Fig. 3(j–k) and Supplementary Fig.S8. According to Ref. [27], $C(r) \propto \exp(-r/\xi)$, where r = the radial distance and ξ = the correlation length which can be obtained through data fitting [27]. Fig. 3(i) displays the correlation lengths obtained from shear strain, volumetric strain, as well as nonaffine displacement. While there is no correlation in the volumetric strain field for the initial several cycles, it increases very quickly after a critical cyclic number of N~10 and, in a few cycles, the correlation length of volumetric strain rises above that of either shear strain or nonaffine displacement. This critical-like behavior suggests that the cyclic loading induced super-plasticity is more likely to be attributed to the rise of volumetric strain or pressure in our model glass. In other words, like other amorphous solids [26], cyclic-induced liquefaction occurs in BMGs also because of the excessive volumetric strain or pressure around local liquid-like sites. Here, we note that a higher strain rate of cyclic deformation, e.g., 10^{11} s^{-1} as shown in Supplementary Fig. S9, fails to rejuvenate the model glass at the same strain magnitude and over the same period of cycling. According to Ref. [10], this is not surprising because of the nature of dynamic heterogeneity in BMGs, i.e., the volume fraction of "liquid-like" atoms reduces remarkably once the external probing time starts to deviate significantly from their intrinsic relaxation time. Here, it may be worth mentioning that the ultrasound induced softening in BMGs is different from the softening behavior of ribbons under ultrasonic vibrations, the latter of which is caused by the excitation of the fast surface dynamics within a very short period of time [15]. However, with respect to the bulk sample, the flow and softening behavior inside the sample is mainly attributed to dynamic heterogeneity and cyclic induced atomic-scale dilations over a longer period of

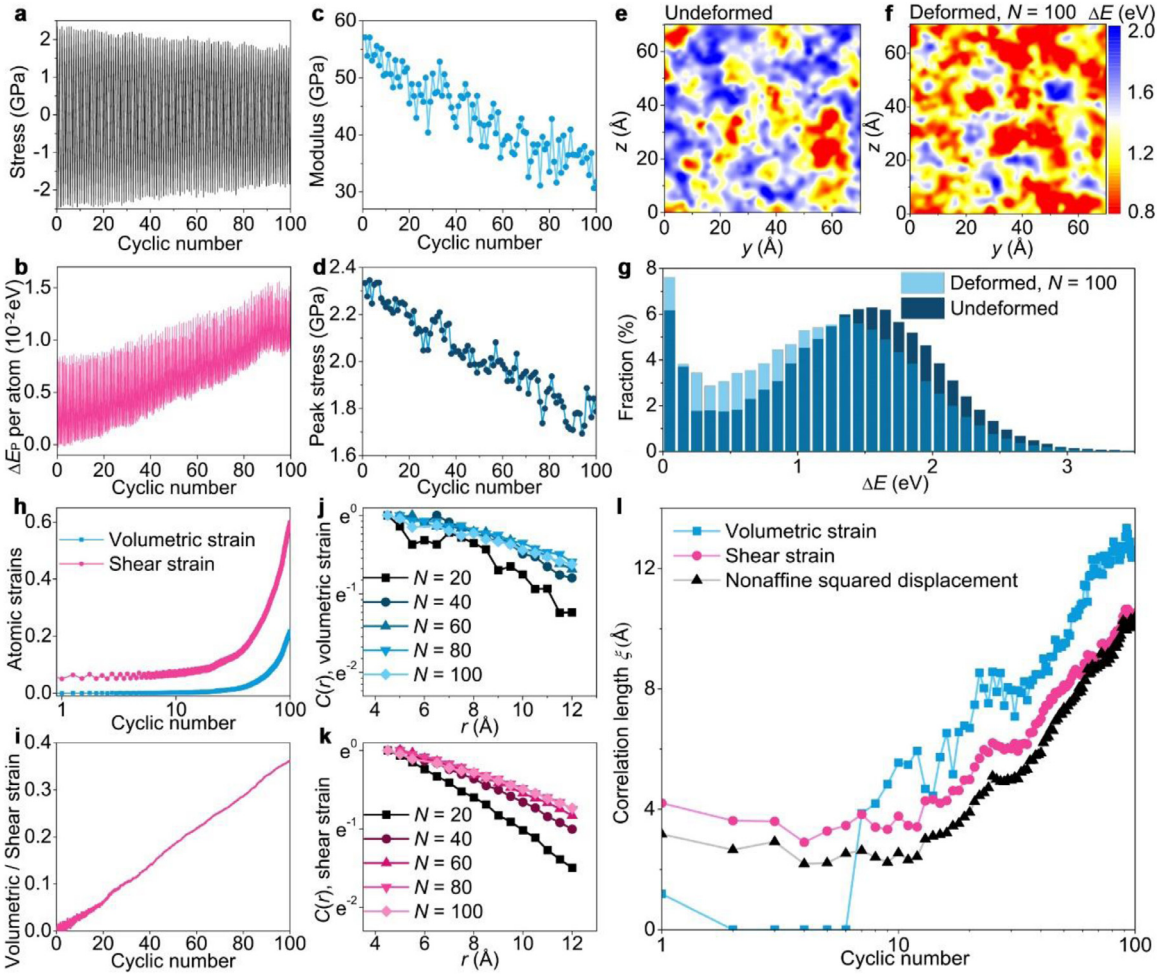

Fig. 3. Evolution of mechanics, thermodynamics, dynamics, and atomic structures of CuZr glass under symmetric tension-compression cyclic loadings. (a–d) Stress–strain curves, potential energy, modulus, and tensile peak stress as a function of cyclic number. (e,f) Contour plots of the activation energies explored in the initial and cyclically deformed samples. (g) The spectra of activation energies. (h,i) Evolutions of atomic-scale volumetric strain, shear strain, and their ratio. (j,k) Spatial autocorrelation functions of the atomic volumetric and shear strains. (l) Variation of the correlation lengths as a function of cyclic number.

time, which leads to significant rejuvenation and final collapse of the solid-like amorphous structure, thereby leading to an overall fluid-like behavior.

Based on our above discussions, now we are at the position to develop a novel processing technique, i.e., UPF, which allows us to perform joining [28], forming, stamping [29] and punching [30] rapidly near room temperature. In doing so, we can effectively mitigate the issue of crystallization and oxidation. As a result, we can now fabricate complicated shapes and geometries from the BMGs not suitable for TPF, such as some Fe-based BMGs with a limited supercooled liquid region [2] but excellent soft magnetic properties and wide applications in electronic devices [31]. As a demonstration, Fig. 4(a) displays a Zr-based BMG plate over 1 mm thick with a semi-circular edge trimmed cleanly by the sonotrode in 0.5 s at a stress level less than 100 MPa. Fig. 4(b) displays a typical stator core for high-speed motors with a fine profile fabricated from the Fe-based amorphous ribbons through the cold shear punching within 0.05 s, much shorter than traditional electron discharge machining (EDM) [32]. Furthermore, BMGs can be cold joined t through UPF, which is due to the combined effect of the super-plasticity and the fast surface dynamics assisted formation of metallic bonding [15] (Fig. 4(c)). Likewise, we can easily fabricate an external thread through the UPF enabled extrusion (Fig. 4(d)) and a thick BMG ring through UPF enabled punching near room temperature, at about 10% of the pressure needed for traditional punching (Fig. 4(e)). In summary, different from the TPF method [7], the outcome of our research now establishes a facile and cost effective UPF method that can be applied to a wide range of BMGs for more applications.

3. Methods

3.1. Alloy casting

In present research, three different typical systems were used, they were $La_{55}Al_{25}Ni_5Cu_{10}Co_5$, $Pd_{40}Cu_{30}P_{20}Ni_{10}$ and $Zr_{35}Ti_{30}Cu_{8.25}Be_{26.75}$ BMG cylinder rods, respectively, prepared by the conventional water cooled copper mold casting process. For the convenience of experiments, the cylinder sample with a diameter of 2 mm was cut into a height of 1.5 mm and polished at two ends.

3.2. X-ray diffraction

The amorphous nature of all the samples in present research was ascertained by the X-ray diffraction (XRD; Rigaku MiniFlex 600) with Cu K_α radiation.

3.3. Scanning electron microscopy

The post-deformation morphologies were examined with the FEI Quanta 450FEG scanning electron microscope (SEM).

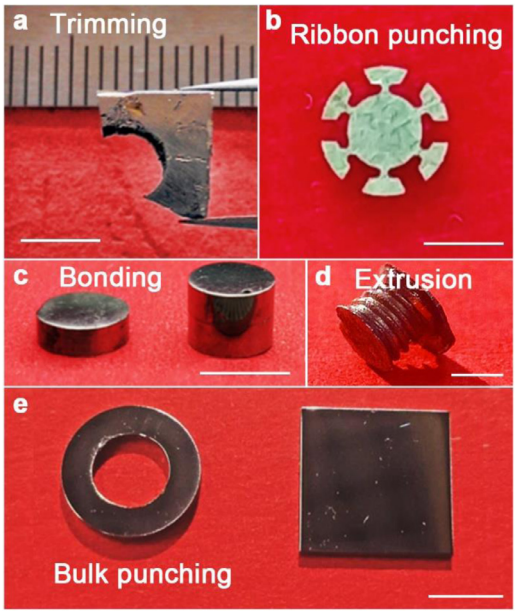

Fig. 4. Potential applications of ultrasonic plasticity of BMGs. (a) Trimming of BMGs with a thickness of more than 1 mm. (b) The punching of metallic glass ribbons (Fe-based) with fine rotor structures. (c) Ultrasonic bonding to manufacture large size of BMGs. (d) External thread fabricated by the instant ultrasonic assisted extrusion forming. (e) Punching of BMGs with thickness > 1 mm. Left is the punched plates with holes, right is the original plate. The scale bar in each subfigure corresponds to 5 mm. All the forming and shaping were conducted under room temperature.

3.4. Transmission electron microscopy

The atomic structure was characterized in a JEM-2100F transmission electron microscopy (TEM). The TEM samples were prepared on a FEI Scios SEM/FIB dual beam system. Firstly, a protective Pt layer (X = 12 μm, Y = 1.5 μm, Z = 0.5 μm) was deposited over the area of interest by electron beam. Another Pt layer with a thickness of 1 μm was deposited on the same area by Ga ion beam. Then, a rectangle lamina was lifted out from the sample and was fixed on a TEM copper grid. A standard thinning procedure was conducted by alternately milling both sides of the lamina with tilting angles of ±1.2° until the thickness of lamina reached to about 100 nm. The final polishing was performed at a reduced ion energy of 2 kV and a current of 27 pA, which minimized the damage to the final thin foil.

3.5. Temperature measurement with a thermocouple

A very thin gauge thermocouple wire coupling with a high rate of data acquisition system (National Instruments, NI, data acquisition frequency is 100 Hz) was used to detect the temperature change during the ultrasonic vibrations on metallic glasses.

3.6. Thermal imaging

The thermal images were collected by the infrared imaging camera (FLIR A325sc) with a data acquisition frequency of 60 Hz.

3.7. Mechanical test

The mechanical performance of metallic glasses after different treatment was measured on the electronic mechanical testing systems (Zwick Roell Z050 TEW) equipped with a laser extensometer.

3.8. Ultrasonic treatment

The schematic setup to conduct ultrasonic plasticity experiment can be seen in Fig. 1(a). The ultrasonic sonotrode is made of cemented carbide (TC4 titanium alloy) and bonded together with a converter or piezoelectric transducer which converts the electrical signal into a mechanical vibration. When in contact with a BMG sample, the sonotrode vibrated at the frequency of 20,000 Hz, leading to BMG liquefaction and super-plastic flows. The total vibration time can be controlled and ranged from milliseconds to seconds.

The vibration amplitude of the sonotrode was 44.4 μm, comprising the machine displacement amplitude d_m and the sample displacement amplitude d_s. To evaluate d_s, the machine stiffness k_m was calculated to be 2.4 × 10^6 N/m according to the load–displacement curve without any sample (See Supplementary Fig. S1a). Since the sample stiffness for BMGs $k_s = ES/L$, where E, $S$and L were the elastic modulus, the area of section and the length of the sample, respectively, one can obtain the following relationship based on Hook's law;

$$\frac{d_s}{d_m} = \frac{k_m}{k_s}$$

By substituting the values of elastic modulus E_{La} = 41.7 GPa, E_{Pd} = 100 GPa, E_{Zr} = 87 GPa into the above equation, we can obtain $d_{s,La}$ = 1140 nm, $d_{s,Pd}$ = 476 nm and $d_{s,Zr}$ = 546 nm for the La-based, Pd-based and Zr-based BMGs, respectively, which leads to the following strain amplitudes applied on the BMG samples: $\varepsilon_{s,La} = 8.1 \times 10^{-4}$, $\varepsilon_{s,Pd} = 3.4 \times 10^{-4}$ and $\varepsilon_{s,Zr} = 3.9 \times 10^{-4}$. As a result, the corresponding stress amplitudes were $\sigma_{s,La} \approx \sigma_{s,Pd} \approx \sigma_{s,Zr} \approx$ 35 MPa, which were far smaller than the corresponding yielding strength of the BMG samples.

3.9. Dynamic modulus mapping

To characterize the reduced modulus, we carried out dynamic modulus mapping (DMM) on the nanoindentation platform (TI-950, Hysitron). During the measurement, a small sinusoidal force was superimposed on the static load, F, and applied to the sample surface together by an indenter with the radius of r. A load transducer kept recording the tip-sample contact stiffness K_s, which in turn can give rise to the elastic modulus according to the classical Hertzian contact theory [33]:

$$E_r = \sqrt{\frac{K_s^2}{6Fr}}$$

In the ideal case where the tip is rotationally symmetric and spherical, and the sample surface is perfectly smooth and flat, the probe radius, r, only correlates to indenter itself under various scanning conditions. However, in practice, one has to take account of the surface-geometry effect on the probe radius. Theoretically, the topological shape of the sample surface is regarded as a two-dimensional array of spherical caps. The influence of surface geometry can be modeled as, $r = r_{tip}r_{surface}/(r_{tip} + r_{surface})$, where $r_{tip}$is the radius curvature of the tip, and $r_{surface}$ is the average radius curvature of the surface. Thereby, a more accurate probe radius can be fitted out by scanning the tip on the standard fused quartz with a known modulus [34].

Following the well-established method [34,35], we scanned a 250 × 250 nm^2 area and obtained the reduced modulus on the BMG samples. During the scanning, a static load of F = 5 μN was applied to the sample surface by a cube corner diamond tip. This value corresponds to a shear stress of ~5 GPa, which is much lower than the critical shear stress (15–30 GPa) for yielding [36,37]. To achieve the best scanning results, the amplitude loads for La-, Pd-,

and Zr-based samples were set at 1.5 μN, 2 μN, and 2 μN, respectively. A load frequency of 200 Hz was applied to ensure a sufficiently large signal-to-noise ratio. Here, it is worth mentioning that we obtained the r_{tip} from the smooth surface of standard fused quartz, keeping the same experiment settings as what we applied to the BMG specimens. The $r_{surface}$ can be determined pixel by pixel based on the topography/height image obtained simultaneously with the contact stiff image, which enabled us to derive the effective probe radius, r. Finally, we could determine the reduced modulus by using this expression.

3.10. Nanoindentation

To further characterize the mechanical properties of the BMG samples, nanoindentation tests (TI-950 Indenter with a 2D-transducer, Hysitron) were conducted on the sample surface at room temperature. The areal function of the Berkovich diamond tip used in this measurement was calibrated on fused quartz firstly. During the experiment, the thermal draft was maintained below 0.2 nm•s^{-1}. Following the Oliver-Pharr's method [38], the apparent hardness (H) and reduced modulus (E_r) of samples were obtained. According to the relationship between Young's modulus (E) and $1/E_r = (1-\upsilon^2)/E + \upsilon_i^2/E_i$, where the modulus and Poisson ratio of the indenter tip, E_i, and ν_i, were taken to be 1141 GPa and 0.07, given that Poisson ratio of sample, ν, should keep being a constant before and after indentation, we obtained the values of E. In Supplementary Table S1, each value was determined from 30to 60 data points by averaging [36,37,39]. Meanwhile, the single indentation experiments with a peak load of 5000 μN and a loading rate of 25 μN•s^{-1} ware also performed on the BMG samples. The corresponding load–displacement curves are displayed on Supplementary Fig. S5.

3.11. Differential scanning calorimetry

To measure the released enthalpy before glass transition, differential scanning calorimetry (DSC 3, METTLER TOLEDO) was carried out at a heating rate of 10 K•min^{-1} in a pure argon atmosphere. Since the heat release associated with structural relaxation spans a wide temperature range up to T_g, our DSC testing started from 50° and ended up after T_g.

3.12. Atomistic simulations

The molecular dynamics were performed on a binary $Cu_{50}Zr_{50}$ model metallic glass system. The force field is described empirically by a widely used Finnis-Sinclair type embedded atom method (EAM) potential [40]. An atomic model system containing 19,652 atoms was prepared with a standard heating-cooling technique from its equilibrium liquid state to ambient temperature at cooling rate of 10^{10} s^{-1}. Periodic conditions were applied to each direction with simulation box of 70 × 70 × 70 Å^3 to represent a bulk metallic glass sample. An isothermal-isobaric ensemble was adopted to guarantee fixed temperature and null pressure in all the cases of simulations [41,42]. To mimic the conditions of supersonic perturbation to the glass sample, we applied a symmetric tension-compression cyclic deformation to the samples with different strain magnitudes from 0.01 to 0.05. The relatively large strain magnitude applied here is targeted to accelerate the mechanical and structural evolutions of the samples within a relatively short atomistic time scale window. We have applied two cases of strain rates in the cyclic loadings, i.e., 10^9 s^{-1} and 10^{10} s^{-1}, to test the influence of the time scale (or frequency) on the structural and mechanical evolution. The structural changes in the samples are characterized by different forms of atomic-scale strains, including atomic von Mises shear strain [43], volumetric strain, and non-affine squared displacement [21]. All the strain patterns are visualized by the software OVITO. The spatial autocorrelation function of the strains is defined as:

$$C_\eta(r) = \frac{\langle \Delta\eta_{r0}\Delta\eta_{r0+r}\rangle - \langle \Delta\eta_{r0}\rangle^2}{\langle \Delta\eta_{r0}^2\rangle - \langle \Delta\eta_{r0}\rangle^2},$$

where η denotes atomic strain, $\Delta\eta = \eta - \bar{\eta}$is the deviation to the ensemble average value $\bar{\eta}$, $r_0$is a reference position where atom resides, and r is the distance away from the central atom. An empirical form of $C(r) \propto \exp(-r/\xi)$is assumed to obtain the spatial correlation length ξ[27], [44].

3.13. Exploration of potential energy landscape

To trace the evolution of the possible flow units during cyclic deformation, an enhanced potential energy landscape (PEL) sampling technique, activation-relaxation technique (ART) [45–47], is performed to exhaustively explore the feature of PEL [48] and the corresponding activation energy for shear transformations event [15]. In this protocol, starting from any local energy basin in the PEL, a cluster of atoms (here with cutoff radius 3.9 Å) is chosen to be perturbated with initial displacement of 0.1 Å on random directions. Then the displacement is pulled along the weakest direction of a Hessian matrix with step of 0.15 Å. Once any eigenvalue of the Hessian matrix is smaller than a critical value of −0.30 eV/Å, the state is pushed toward to the saddle point by Lanczos algorithm. The calculations are stopped if the maximum force of the system is smaller than 0.05 eV/Å. The energy different between the saddle configuration and the initial configuration is defined as the activation energy of a structural rearrangement. For each activated cluster, 10 cases of successful event are searched to make a total number of 196,520 events, in either the unformed or the cyclically deformed glass sample.

Author contributions

J.M. Y.J.W. and Y.Y. conceived the idea. W.H.W, J.M. and Y.Y. supervised the work. X.L. and Z.L. carried out ultrasonic experiments, thermal imagining, XRD and compression tests at high temperatures. J.Y.Z. and Q.F.H. performed nanoindentation, modulus mapping, DSC and TEM. T.Y.W. carried out theoretical modeling. D.W and Y.J.W. did the atomistic simulations. J.M., X.L., J.Y.Z., T.Y.W., X.D.L., Y.Y., and Y.J.W. wrote the manuscript. All authors contributed to the discussion and analysis of the results.

Data and materials availability

All data needed to evaluate the conclusions in the paper are present in the paper and/or the Supplementary Materials. Additional data related to this paper may be requested from the authors.

Declaration of Competing Interest

The authors declare no competing financial interest.

Acknowledgments

The work was supported by the Key Basic and Applied Research Program of Guangdong Province, China (Grant Nr. 2019B030302010), the NSF of China (Grant No.. 51871157), the Science and Technology Innovation Commission Shenzhen (Grants No. JCYJ20170412111216258), the National Key Research and Development Program of China (Grant No. 2018YFA0703604). YJW was

supported by the NSFC (Grant No. 11672299) and the Youth Innovation Promotion Association of Chinese Academy of Sciences (Grant No. 2017025). YY was supported by Research Grant Council (RGC), Hong Kong Government, through General Research Fund (RGC) with the grant numbers CityU11213118, CityU11200719 and CityU11209317. The authors also thank the assistance on microscope observation received from the Electron Microscope Center of the Shenzhen University.

Supplementary materials

Supplementary material associated with this article can be found, in the online version, at doi:10.1016/j.apmt.2020.100866.

References

[1] M. Ashby, A. Greer, Metallic glasses as structural materials, Scr. Mater. 54 (3) (2006) 321.
[2] A. Inoue, A. Takeuchi, Recent development and application products of bulk glassy alloys, Acta Mater. 59 (6) (2011) 2243.
[3] G. Kumar, et al., Nanomoulding with amorphous metals, Nature 457 (7231) (2009) 868.
[4] A.L. Greer, Metallic glasses, Science 267 (5206) (1995) 1947.
[5] A.L. Greer, et al., Shear bands in metallic glasses, Mater. Sci. Eng.: R: Rep. 74 (4) (2013) 71.
[6] C.A. Schuh, et al., Mechanical behavior of amorphous alloys, Acta Mater. 55 (12) (2007) 4067.
[7] J. Schroers, Processing of Bulk Metallic Glass, Adv. Mater. 22 (14) (2010) 1566.
[8] Y. Huang, et al., Shear punching of a Ti-based bulk metallic glass, Mater. Sci. Eng., A 561 (2013) 220.
[9] K. Efimenko, et al., Nested self-similar wrinkling patterns in skins, Nat. Mater. 4 (4) (2005) 293.
[10] J.C. Qiao, et al., Structural heterogeneities and mechanical behavior of amorphous alloys, Prog. Mater. Sci. 104 (2019) 250.
[11] Y. Yokoyama, et al., Malleable hypoeutectic Zr–Ni–Cu–Al bulk glassy alloys with tensile plastic elongation at room temperature, Philos. Mag. Lett. 89 (5) (2009) 322.
[12] W.L. Johnson, K. Samwer, A Universal Criterion for Plastic Yielding of Metallic Glasses with a Temperature Dependence, Phys. Rev. Lett. 95 (19) (2005) 195501.
[13] K. Zhao, et al., Room temperature homogeneous flow in a bulk metallic glass with low glass transition temperature, Appl. Phys. Lett. 98 (14) (2011) 141913.
[14] L.S. Huo, et al., The dependence of shear modulus on dynamic relaxation and evolution of local structural heterogeneity in a metallic glass, Acta Mater. 61 (12) (2013) 4329.
[15] J. Ma, et al., Fast surface dynamics enabled cold joining of metallic glasses, Sci. Adv. 5 (11) (2019) eaax7256.
[16] Q. Wang, et al., Universal secondary relaxation and unusual brittle-to-ductile transition in metallic glasses, Mater. Today 20 (6) (2017) 293.
[17] A. Argon, Plastic deformation in metallic glasses, Acta Metall. 27 (1) (1979) 47.
[18] Y. Sun, et al., Thermomechanical processing of metallic glasses: extending the range of the glassy state, Nat. Rev. Mater. 1 (9) (2016) 16039.
[19] J. Pan, et al., Strain-hardening and suppression of shear-banding in rejuvenated bulk metallic glass, Nature 578 (7796) (2020) 559.
[20] S.V. Ketov, et al., Rejuvenation of metallic glasses by non-affine thermal strain, Nature 524 (7564) (2015) 200.
[21] S.-.C. Lee, et al., Microstructural evolution of an elastostatically compressed amorphous alloy and its influence on the mechanical properties, Scr. Mater. 58 (7) (2008) 591.
[22] D. Louzguine-Luzgin, et al., On room-temperature quasi-elastic mechanical behaviour of bulk metallic glasses, Acta Mater. 129 (2017) 343.
[23] M. Zhang, et al., Mechanical relaxation-to-rejuvenation transition in a Zr-based bulk metallic glass, Sci. Rep. 7 (1) (2017) 1.
[24] J. Pan, et al., Extreme rejuvenation and softening in a bulk metallic glass, Nat. Commun. 9 (1) (2018) 560.
[25] M. Falk, J. Langer, Dynamics of viscoplastic deformation in amorphous solids, Phys. Rev. E 57 (6) (1998) 7192.
[26] S.A. Galindo-Torres, et al., Micromechanics of liquefaction in granular materials, Phys. Rev. Appl. 10 (6) (2018) 064017.
[27] E.D. Cubuk, et al., Structure-property relationships from universal signatures of plasticity in disordered solids, Science 358 (6366) (2017) 1033.
[28] X. Li, et al., Cold joining to fabricate large size metallic glasses by the ultrasonic vibrations, Scr. Mater. 185 (2020) 100.
[29] Z. Li, et al., Forming of metallic glasses: mechanisms and processes, Mater. Today Adv. 7 (2020) 100077.
[30] F. Luo, et al., Ultrasonic assisted micro-shear punching of amorphous alloy, Mater. Res. Lett. 6 (10) (2018) 545.
[31] Y. Yoshizawa, et al., Common mode choke cores using the new Fe-based alloys composed of ultrafine grain structure, J. Appl. Phys. 64 (10) (1988) 6044.
[32] S.H. Yeo, et al., Processing of zirconium-based bulk metallic glass (BMG) using micro electrical discharge machining (Micro-EDM), Mater. Manuf. Process. 24 (12) (2009) 1242.
[33] Syed Asif, S. A., et al., Quantitative imaging of nanoscale mechanical properties using hybrid nanoindentation and force modulation, J. Appl. Phys. 90 (3) (2001) 1192.
[34] H. Wagner, et al., Local elastic properties of a metallic glass, Nat. Mater. 10 (2011) 439.
[35] N.X. Randall, et al., Nanoindentation analysis as a two-dimensional tool for mapping the mechanical properties of complex surfaces, J. Mater. Res. 24 (3) (2009) 679.
[36] W.H. Wang, Correlations between elastic moduli and properties in bulk metallic glasses, J. Appl. Phys. 99 (9) (2006) 093506.
[37] N. Li, et al., The indentation size effect in Pd40Cu30Ni10P20 bulk metallic glass, J. Phys. D Appl. Phys. 41 (15) (2008) 155415.
[38] W.C. Oliver, G.M. Pharr, An improved technique for determining hardness and elastic modulus using load and displacement sensing indentation experiments, J. Mater. Res. 7 (06) (1992) 1564.
[39] G. Duan, et al., Bulk metallic glass with benchmark thermoplastic processability, Adv. Mater. 19 (23) (2007) 4272.
[40] M.I. Mendelev, et al., Development of suitable interatomic potentials for simulation of liquid and amorphous Cu–Zr alloys, Philos. Mag. 89 (11) (2009) 967.
[41] S. Nosé, A molecular dynamics method for simulations in the canonical ensemble, Mol. Phys. 52 (2) (1984) 255.
[42] M. Parrinello, A. Rahman, Polymorphic transitions in single crystals: A new molecular dynamics method, J. Appl. Phys. 52 (12) (1981) 7182.
[43] F. Shimizu, et al., Theory of shear banding in metallic glasses and molecular dynamics calculations, Mater. Trans. 48 (11) (2007) 2923.
[44] D. Wei, et al., Revisiting the structure–property relationship of metallic glasses: Common spatial correlation revealed as a hidden rule, Phys. Rev. B 99 (1) (2019) 014115.
[45] G.T. Barkema, N. Mousseau, Event-based relaxation of continuous disordered systems, Phys. Rev. Lett. 77 (21) (1996) 4358.
[46] R. Malek, N. Mousseau, Dynamics of Lennard-Jones clusters: A characterization of the activation-relaxation technique, Phys. Rev. E 62 (6) (2000) 7723.
[47] E. Machado-Charry, et al., Optimized energy landscape exploration using the *ab initio* based activation-relaxation technique, J. Chem. Phys. 135 (3) (2011) 034102.
[48] P.G. Debenedetti, F.H. Stillinger, Supercooled liquids and the glass transition, Nature 410 (6825) (2001) 259.